Effect of precipitate shape and orientation on Orowan strengthening of non-basal slip modes in hexagonal crystals, application to magnesium alloys

Fulin Wang *, Jishnu J. Bhattacharyya, Sean R. Agnew

Department of Materials Science and Engineering, University of Virginia, Charlottesville, VA 22904, U.S.A.

* Corresponding author. Tel.: +14342974850; fax: +14349825660; email: fw8yc@virginia.edu.

Abstract

Orowan equations predicting the strengthening of non-basal slip systems in hexagonal crystals are derived for rationally distributed, shear resistant precipitates of typical morphologies and orientations. These equations may be employed for any hexagonal crystal, but application is made specifically to hexagonal close packed Mg, where alloy development is presently quite active. Particular focus is placed on discerning the effect on $\langle c+a \rangle$ dislocations, and generally speaking, $\langle c+a \rangle$ slip is most potently strengthened by prismatic plate shaped precipitates, as was shown previously for basal and prismatic slip. If strengthening is the primary goal, prismatic plate shaped precipitates appear ideal. Because the motion of $\langle c+a \rangle$ dislocations has been repeatedly emphasized as crucial for preserving ductility, it may be of interest to consider.

Keywords: magnesium alloys; precipitate; Orowan strengthening; non-basal slip.

1. Introduction

Precipitation hardening is a promising mechanism for developing high strength magnesium alloys [1, 2, 3, 4, 5]. In common precipitation hardenable Mg alloys, the precipitate types and morphologies have been studied extensively by experimental methods, including the quantitative characterization of size and distribution [6, 7, 8]. The theoretical evaluations of the

strengthening effects of precipitates on basal and prismatic slip systems were developed by Nie [9] and Robson [10], respectively, based on the Orowan mechanism.

Whereas the activation of basal slip is associated with the microscopic yield stress, even in randomly textured cast material, the slip activity of non-basal slip of $\langle a \rangle$ and $\langle c + a \rangle$ dislocations affects the flow stress and hardening behavior at higher strain levels [11]. Recently, it has been confirmed that the $\{10\bar{1}2\}$ twins in Mg alloys contain abundant $\langle c + a \rangle$ dislocations due to the dislocation transmutation mechanism [12, 13]. It is therefore of interest to study the strengthening effect of precipitates on the non-basal $\langle c + a \rangle$ slip systems. The $\langle c + a \rangle$ slip system was reported to be strengthened only modestly by the prismatic plates in a WE43 alloy via in-situ neutron diffraction and plasticity modeling [11], and weakly affected by c-axis rods in Mg-5%Zn single crystals examined via micropillar compression tests [7]. A quantitative evaluation is needed in order to predict and compare the relative strengthening effects of differently shaped precipitates.

For precipitates of different phase and size, the entire population of precipitates does not always fall in the single regime of dislocations cutting or bowing. Quantifying the strengthening effect due to either mechanism necessitates geometric parameters such as the inter-particle spacing and precipitate size encountered by gliding dislocations on the slip plane [14]. If dislocations are able to cut through precipitates, it is often assumed that the slip plane is continuous for dislocation with identical Burgers vector between matrix and precipitate [1]. Such assumption was made for the evaluation of basal dislocation cutting prismatic precipitate plates [1], but it is difficult to assess the situation for non-basal dislocations due to the lack of structural information regarding their propensity to shear precipitates. The current paper presents the Orowan equations for the non-basal slip systems in Mg alloys, due to rationally distributed, shear resistant precipitates of typical morphologies and orientations. Note that the general forms of these equations, which may be employed for any hexagonal crystal, are presented in the paper. However, application is made to Mg, where alloy development is presently quite active. Furthermore, the geometric parameters derived here, e.g. center-to-center distance of precipitates, are also applicable for any subsequent, quantitative evaluation of the strengthening effect of shearable precipitates.

2. Orowan strengthening

The increase in the critical resolved shear stress (CRSS) of a slip system due to dispersoids is given by

$$\Delta\tau = \frac{Gb}{2\pi\sqrt{1-\nu}}\frac{1}{\lambda}\ln\frac{d_P}{r_0}, \quad (1)$$

where $\Delta\tau$ is the increase in CRSS of the selected slip system due to precipitation strengthening, G is the shear modulus, b the Burgers vector of dislocation, ν the Poisson ratio, λ the effective planar inter-particle spacing, d_P the mean planar diameter of the precipitate, and r_0 the core radius of dislocation, which is conveniently assumed as b in this work. In Eq. (1), λ and d_P vary with the shape and orientation of the precipitate with respect to different slip planes. They are invariant if precipitates are in spherical shape, i.e. isotropic strengthening arises. Assuming uniform diameter D and a triangular array distribution on the slip plane, the increment in CRSS due to spherical precipitates with volume fraction f is [9]

$$\Delta\tau = \frac{Gb}{2\pi\sqrt{1-\nu}}\frac{1}{\left(\frac{0.779}{\sqrt{f}}-0.785\right)D}\ln\frac{0.785\,D}{b}. \quad (2)$$

In this work, four types of commonly observed precipitates in Mg alloys are considered: (1) $\{10\bar{1}0\}$ prismatic plates, (2) $\{11\bar{2}0\}$ prismatic plates, (3) (0001) basal plates and (4) $[0001]$ c-axis rods. The resultant increments in CRSS ($\Delta\tau$) of the non-basal slip systems are estimated, including the slip of $\langle c+a\rangle$ dislocations on second-order pyramidal (Py-2) planes $\{11\bar{2}2\}$ and first-order pyramidal (Py-1) planes $\{10\bar{1}1\}$, as well as $\langle a\rangle$ dislocations on Py-1 planes and first-order prismatic (Pr.) planes $\{10\bar{1}0\}$.

The plate- and rod-shaped precipitates are assumed to have uniform diameter D and thickness/ length T at volume fraction f. According to Fullman [15], the number density of precipitate per volume N_V and per area N_A are calculated by Eq. (3) and (4), given below. P is the probability a plane intersects a precipitate, and it equals $D\sin\varphi$ for plates and $T\cos\varphi$ for rods, where φ is the angle between the normal direction of slip plane and that of precipitate habit plane or rod axis direction. N_A is thusly obtained for plates and rods as presented in Eq. (5)

$$N_A = N_V\,P \quad (3)$$

$$f = N_V\,V = N_V\,\pi D^2 T/4 \quad (4)$$

$$N_{A-Plate} = \frac{4f}{\pi DT}\sin\varphi\,;\;\; N_{A-Rod} = \frac{4f}{\pi D^2}\cos\varphi \quad (5)$$

The relations between the planar number density N_A and planar center-to-center distance of precipitates l_P, and thereafter l_P and effective inter-particle spacing λ depend on the distribution of the projections of the intersected precipitates on slip plane. As will be introduced subsequently, in some cases there are more than one planar variant of the intersected precipitates on a selected slip plane. For the purpose of comparison and representation of all planar variants of precipitates, an equilateral triangular array distribution on slip plane is assumed, and λ takes the value of the mean average of the distances between the nearest neighbor precipitates.

The projections of the intersected plate- and rod-shaped precipitates on the slip plane are represented by three shapes: rectangle, circle and ellipse. An effective length of the intersected precipitate is calculated as the mean planar diameter d_P in the logarithmic term of Eq. (1).

2.1 $\{10\bar{1}0\}$ precipitate plates

2.1.1 Second-order pyramidal slip plane $\{11\bar{2}2\}$

Figure 1(a) and (b) present schematically the fact that projections of the intersected $\{10\bar{1}0\}$ plate precipitates on $\{11\bar{2}2\}$ slip planes have two variants in rectangular shape. Firstly, there are two values of the angle (φ) between the precipitate habit plane and the slip plane, namely φ_1 between $(1\bar{1}00)$ and $(11\bar{2}2)$, and φ_2 between $(10\bar{1}0)$, $(01\bar{1}0)$ and $(11\bar{2}2)$. While the mean planar diameter of the precipitates is the same for all variants, $D_P = \pi/4\ D$, the projected planar thickness is different, $T_P = T/\sin\varphi$. Secondly, the major axes of the projections of the precipitates constitute an isosceles triangle with base angle θ. It leads to different planar inter-particle spacings λ_1 and λ_2. Consequently, gliding dislocations on the slip plane experience two types of precipitates with different dimensions and inter-particle spacings. The two sets of values are accounted for by assigning the probabilities of $2/3$ and $1/3$. The geometric parameters φ_1, φ_2 and θ vary for different cases of intersecting precipitate habit plane and slip plane. Equations for calculation in hexagonal lattices with various c/a ratios are provided in the Appendix. The values of these geometric parameters for the c/a ratio of Mg are specifically listed in Appendix, Table 1, and will be used in the rest of the paper.

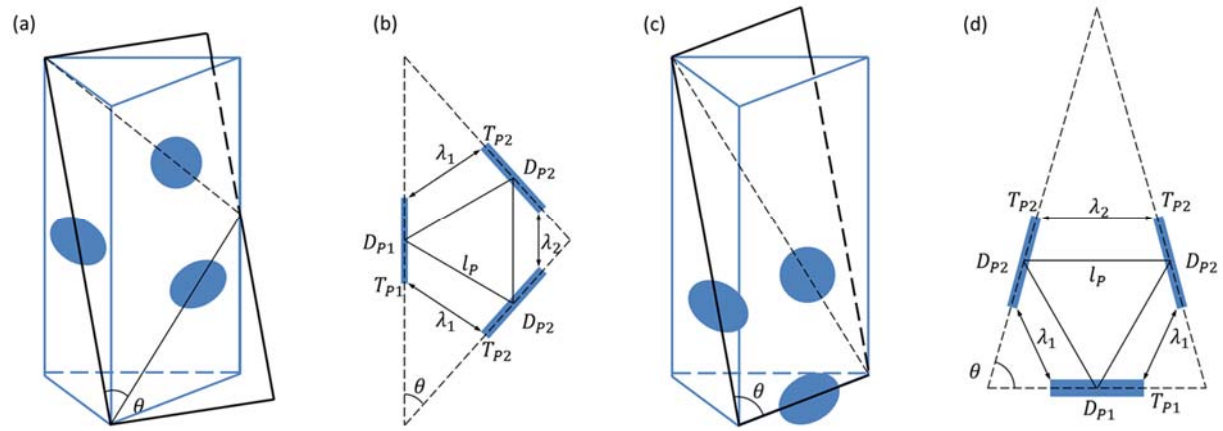

Figure 1. Precipitate plates on $\{10\bar{1}0\}$ planes are intersected by slip plane (a) $(11\bar{2}2)$ and (c) $(10\bar{1}1)$ respectively. (b) Projection of the intersected precipitates on the $(11\bar{2}2)$ plane. (c) Projection of the intersected precipitates on the $(10\bar{1}1)$ plane. The precipitates are assumed to distribute in an equilateral triangular array on the slip plane.

For the geometry depicted in Figure 1(b), the planar center-to-center distance of precipitates l_P and two shortest inter-particle spacings λ_1 and λ_2 are expressed as

$$l_P = \left(\frac{1}{\frac{8f}{3\sqrt{3}\pi DT}(\sin\varphi_1 + 2\sin\varphi_2)}\right)^{\frac{1}{2}}, \tag{6}$$

$$\lambda_1 = l_p - \left[\frac{1}{4} + \frac{\cos(120°-\theta)}{2}\right] D_P - \left[\frac{\sqrt{3}/2}{\sin\varphi_1} + \frac{\sin(120°-\theta)}{\sin\varphi_2}\right] T, \tag{7}$$

$$\lambda_2 = l_P - \cos\theta\ D_P - \frac{\sin\theta}{\sin\varphi_2}\ T, \tag{8}$$

and the effective inter-particle spacing takes the mean average value

$$\lambda_{eff} = \frac{2}{3}\lambda_1 + \frac{1}{3}\lambda_2. \tag{9}$$

The effective length of the intersected precipitate is calculated as

$$d_P = \sqrt{\overline{D_P\,T_P}} = \sqrt{\frac{\pi}{4}\left(\frac{2}{3}\frac{1}{\sin\varphi_2} + \frac{1}{3}\frac{1}{\sin\varphi_1}\right) DT}. \tag{10}$$

This set of equations applies to all the cases where prismatic precipitate plane is intersected by pyramidal slip plane.

In the case of Py-2 slip intersecting $\{10\bar{1}0\}$ oriented precipitates, $\varphi_1 = 90°$, $\varphi_2 = 42.5°$ and $\theta = 42.24°$ in Mg, the planar inter-particle spacings are calculated as

$$\lambda_1 = 0.932\sqrt{\frac{DT}{f}} - 0.280\,D - 2.313\,T, \tag{11}$$

$$\lambda_2 = 0.932\sqrt{\frac{DT}{f}} - 0.581\,D - 0.995\,T \text{ and} \tag{12}$$

$$\lambda_{eff} = 0.9317\sqrt{\frac{DT}{f}} - 0.3802\,D - 1.8737\,T, \tag{13}$$

and the increment in the CRSS of $\langle c+a \rangle$ dislocation slip on Py-2 plane is

$$\Delta\tau = \frac{Gb}{2\pi\sqrt{1-\nu}} \frac{1}{0.932\sqrt{\frac{DT}{f}} - 0.380\,D - 1.874\,T} \ln\frac{1.018\sqrt{DT}}{r_0}. \tag{14}$$

2.1.2 First-order pyramidal slip plane $\{10\bar{1}1\}$

The geometry of $\{10\bar{1}0\}$ precipitate planes intersected by Py-1 slip is depicted in Figure 1(c) and (d). The equations Eq. (6-10) are employed with angular values $\varphi_1 = 28.1°$, $\varphi_2 = 63.8°$ and $\theta = 74.8°$. The planar inter-particle spacings are

$$\lambda_1 = 0.949\sqrt{\frac{DT}{f}} - 0.473\,D - 2.631\,T, \tag{15}$$

$$\lambda_2 = 0.949\sqrt{\frac{DT}{f}} - 0.206\,D - 1.075\,T \text{ and} \tag{16}$$

$$\lambda_{eff} = 0.949\sqrt{\frac{DT}{f}} - 0.384\,D - 2.113\,T, \tag{17}$$

and the increment in the CRSS of $\langle c+a \rangle$ or $\langle a \rangle$ dislocation slip on Py-1 plane is

$$\Delta\tau = \frac{Gb}{2\pi\sqrt{1-\nu}} \frac{1}{0.949\sqrt{\frac{DT}{f}} - 0.384\,D - 2.113\,T} \ln\frac{1.068\sqrt{DT}}{r_0}. \tag{18}$$

2.1.3 Prismatic slip plane

When plate-shaped precipitates on the $\{10\bar{1}0\}$ planes are intersected by the prismatic slip (Figure 2a and b), there is no dependence on c/a ratio (i.e. the relations can be immediately applied to Mg, Ti, Zr or any other hexagonal crystal). The projections of the intersected precipitates have two variants: a rectangle with length $D_{P2} = \pi/4\,D$ and thickness $T_{P2} = T/\sin 60° = 1.155\,T$, and a disk with diameter D. Assuming an equilateral triangular array distribution of the intersected precipitate on slip plane, the particle center-to-center spacing is

$$l_P = \left(\frac{2\sqrt{3}\,\pi D^2 T}{4f\,(T+\sqrt{3}\,D)}\right)^{\frac{1}{2}} = 1.650\sqrt{\frac{D^2 T}{f(T+1.732D)}} \tag{19}$$

The planar inter-particle spacings λ_1, λ_2 and the averaged λ are

$$\lambda_1 = l_P - \frac{D}{2} - \frac{\pi}{8}D, \tag{20}$$

$$\lambda_2 = l_P - \frac{2}{\sqrt{3}}T \text{ and} \tag{21}$$

$$\lambda_{eff} = \frac{2}{3}\lambda_1 + \frac{1}{3}\lambda_2 = 1.650\sqrt{\frac{D^2 T}{f(T+1.732D)}} - 0.595\,D - 0.385\,T. \tag{22}$$

The effective length of the intersected precipitate is calculated by

$$d_P = 0.635\sqrt{DT} + 0.333\,D \tag{23}$$

and the increment in the CRSS of $\langle a \rangle$ dislocation slip on prismatic plane is

$$\Delta\tau = \frac{Gb}{2\pi\sqrt{1-\nu}} \frac{1}{1.650\sqrt{\frac{D^2 T}{f(T+1.732D)}} - 0.595\,D - 0.385\,T} \ln\frac{0.635\sqrt{DT}+0.333\,D}{r_0}. \tag{24}$$

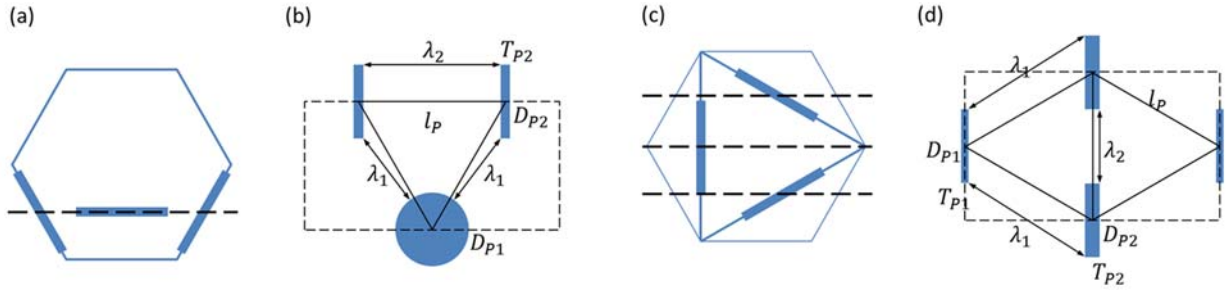

Figure 2. Precipitate plates on (a) $\{10\bar{1}0\}$ planes and (c) $\{11\bar{2}0\}$ planes are intersected by slip plane $(10\bar{1}0)$ viewing perpendicular to the (0001) basal plane. (b) Projection of the intersected $\{10\bar{1}0\}$ precipitates on the slip plane. (d) Projection of the intersected $\{11\bar{2}0\}$ precipitates on the slip plane. The precipitates are assumed to distribute in an equilateral triangular array on the slip plane.

2.2 $\{11\bar{2}0\}$ precipitate plates

For precipitate plates on the $\{11\bar{2}0\}$ planes, their projected intersections on Py-2 or Py-1 slip planes also involve two variants with different sizes and directions, the geometry is similar to that depicted in Figure 1. As such, equations Eq. (6-10) are employed by using their respective angles to compute the CRSS increment.

2.2.1 Second-order pyramidal plane $\{11\bar{2}2\}$

The interplanar angles and the base angle of the isosceles triangle are $\varphi_1 = 31.6°$, $\varphi_2 = 64.8°$ and $\theta = 73.2°$, the planar inter-particle spacing is calculated from

$$\lambda_1 = 0.935\sqrt{\frac{DT}{f}} - 0.465\,D - 2.458\,T, \tag{25}$$

$$\lambda_2 = 0.935\sqrt{\frac{DT}{f}} - 0.228\,D - 1.058\,T \text{ and} \tag{26}$$

$$\lambda_{eff} = 0.935\sqrt{\frac{DT}{f}} - 0.386\,D - 1.991\,T, \tag{27}$$

and the increment in the CRSS of $\langle c + a \rangle$ dislocation slip on Py-2 plane is

$$\Delta\tau = \frac{Gb}{2\pi\sqrt{1-\nu}} \frac{1}{0.935\sqrt{\frac{DT}{f}} - 0.386\,D - 1.991\,T} \ln\frac{1.038\sqrt{DT}}{r_0}. \tag{28}$$

2.2.2 First-order pyramidal plane $\{10\bar{1}1\}$

The angles between planes and the base angle of the isosceles triangle are $\varphi_1 = 90°$, $\varphi_2 = 40.2°$ and $\theta = 39.2°$, the effective planar inter-particle spacing is calculated as

$$\lambda_1 = 0.944\sqrt{\frac{DT}{f}} - 0.259\,D - 2.397\,T, \tag{29}$$

$$\lambda_2 = 0.944\sqrt{\frac{DT}{f}} - 0.609\,D - 0.979\,T \text{ and} \tag{30}$$

$$\lambda = 0.944\sqrt{\frac{DT}{f}} - 0.376\,D - 1.924\,T, \tag{31}$$

and the increment in the CRSS Of $\langle c + a \rangle$ or $\langle a \rangle$ dislocation slip on Py-1 plane is

$$\Delta\tau = \frac{Gb}{2\pi\sqrt{1-\nu}} \frac{1}{0.944\sqrt{\frac{DT}{f}} - 0.376\,D - 1.924\,T} \ln\frac{1.036\sqrt{DT}}{r_0}. \tag{32}$$

2.2.3 Prismatic slip plane

The projections of the intersected plate-shaped precipitates on $\{11\bar{2}0\}$ planes by first-order prismatic slip planes are parallel rectangles (Figure 2c and d). Since the precipitate habit planes intersect the slip plane at two angles $\varphi_1 = 90°$ and $\varphi_2 = 30°$ (which are independent on

c/a ratio), there are two variants whose length and thickness are given by $D_P = \pi/4\ D$, $T_P = T/\sin\varphi$. The expressions for l_P and λ are as follows.

$$l_P = \sqrt{\frac{\sqrt{3}\pi DT}{4f}} = 1.166\sqrt{\frac{DT}{f}} \tag{33}$$

$$\lambda_1 = \sqrt{\left(l_p \sin 60° - \frac{1/\sin\varphi_1 + 1/\sin\varphi_2}{2}\ T\right)^2 + \left(l_p \cos 60°\right)^2} \tag{34}$$

$$\lambda_2 = l_p - \frac{\pi}{4}D \tag{35}$$

$$\lambda = \frac{2}{3}\lambda_1 + \frac{1}{3}\lambda_2 = \sqrt{0.605\frac{DT}{f} - 1.346\ T\sqrt{\frac{DT}{f}} + T^2} + 0.389\sqrt{\frac{DT}{f}} - 0.262D \tag{36}$$

The mean planar diameter of the obstacle is calculated using Eq. (10), and the increment in the CRSS of $\langle a \rangle$ dislocation slip on prismatic plane is

$$\Delta\tau = \frac{Gb}{2\pi\sqrt{1-\nu}} \frac{1}{\sqrt{0.605\frac{DT}{f} - 1.346\ T\sqrt{\frac{DT}{f}} + T^2} + 0.389\sqrt{\frac{DT}{f}} - 0.262D} \ln\frac{1.144\sqrt{DT}}{r_0}. \tag{37}$$

2.3 (0001) precipitate plates

2.3.1 Second-order pyramidal slip plane $\{11\bar{2}2\}$

When the basal plates are intersected by the pyramidal slip planes, the intersections on the slip plane are parallel rectangles. An example is presented in Figure 3(a) and (b) for the case of basal plates intersected by Py-2 plane. The intersections have the same length $D_P = \pi/4$, and thickness $T_P = T/\sin\varphi$. The generic expressions for l_P and λ are

$$l_P = \sqrt{\frac{\pi DT}{2\sqrt{3}f\sin\varphi}}, \tag{38}$$

$$\lambda_1 = \sqrt{\left(l_p \sin 60° - \frac{T}{\sin\varphi}\right)^2 + \left(l_p \cos 60°\right)^2}, \tag{39}$$

$$\lambda_2 = l_P - \frac{\pi}{4}\ D, \text{ and} \tag{40}$$

$$\lambda_{eff} = \frac{2}{3}\lambda_1 + \frac{1}{3}\lambda_2. \tag{41}$$

The mean planar diameter of the obstacle is calculated by

$$d_P = \sqrt{D_P\ T_P} = \sqrt{\frac{\pi}{4}\ \frac{1}{\sin\varphi}DT} \tag{42}$$

In the case of basal plates intersected by Py-2 plane, $\varphi = 45.6°$, we obtain

$$\lambda = \sqrt{0.564\frac{DT}{f} - 1.212\,T\sqrt{\frac{DT}{f}} + 0.869\,T^2} + 0.375\sqrt{\frac{DT}{f}} - 0.262D \text{ and} \tag{43}$$

$$\Delta\tau = \frac{Gb}{2\pi\sqrt{1-\nu}} \frac{1}{\sqrt{0.564\frac{DT}{f} - 1.212\,T\sqrt{\frac{DT}{f}} + 0.869\,T^2} + 0.375\sqrt{\frac{DT}{f}} - 0.262D} \ln\frac{1.048\sqrt{DT}}{r_0}. \tag{44}$$

2.3.2 First-order pyramidal slip plane $\{10\bar{1}1\}$

In this case, employing the same set of equations Eq. (38-42), and using the angle $\varphi = 51.1°$, the effective planar inter-particle spacing and increment in CRSS are given by

$$\lambda = \sqrt{0.518\frac{DT}{f} - 1.067\,T\sqrt{\frac{DT}{f}} + 1.649\,T^2} + 0.360\sqrt{\frac{DT}{f}} - 0.262D \text{ and} \tag{45}$$

$$\Delta\tau = \frac{Gb}{2\pi\sqrt{1-\nu}} \frac{1}{\sqrt{0.518\frac{DT}{f} - 1.067\,T\sqrt{\frac{DT}{f}} + 1.649\,T^2} + 0.360\sqrt{\frac{DT}{f}} - 0.262D} \ln\frac{1.004\sqrt{DT}}{r_0}. \tag{46}$$

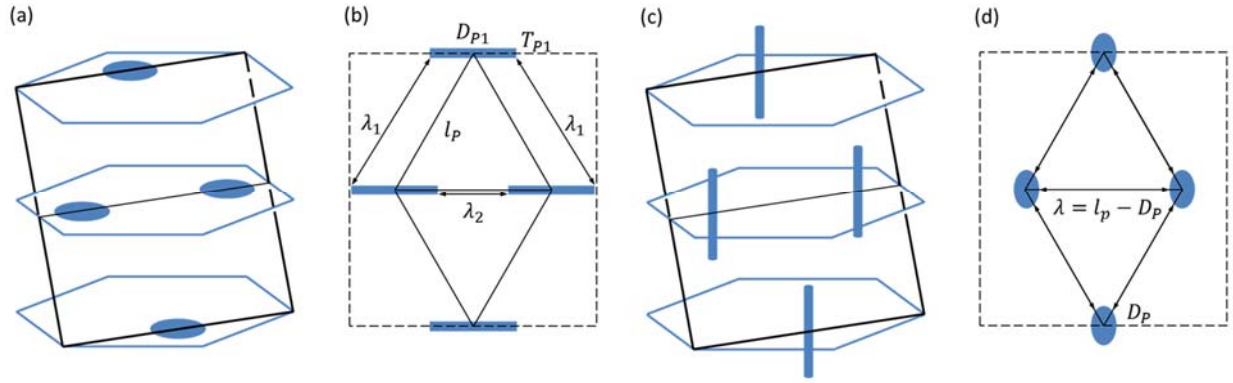

Figure 3. (a) Precipitate plates on (0001) planes and (c) $[0001]$ rods are intersected by slip plane $\{11\bar{2}2\}$. (b) and (d) are projections of the intersected precipitates on the slip plane. The precipitates are assumed to distribute in an equilateral triangular array on the slip plane.

2.3.3 Prismatic slip plane

The prismatic slip planes are perpendicular to the basal precipitate plane, i.e. $\varphi = 90°$, the expressions for λ and $\Delta\tau$ are

$$\lambda = \sqrt{0.403\frac{DT}{f} - 0.733\,T\sqrt{\frac{DT}{f}} + T^2} + 0.317\sqrt{\frac{DT}{f}} - 0.262D \text{ and} \tag{47}$$

$$\Delta\tau = \frac{Gb}{2\pi\sqrt{1-\nu}} \frac{1}{\sqrt{0.403\frac{DT}{f} - 0.733\,T\sqrt{\frac{DT}{f}} + T^2} + 0.317\sqrt{\frac{DT}{f}} - 0.262D} \ln\frac{0.886\sqrt{DT}}{r_0}. \tag{48}$$

2.4 [0001] precipitate rods

2.4.1 Second-order pyramidal slip plane $\{11\bar{2}2\}$

The probability of c-axis rods being intersected by the inclined pyramidal slip plane is $P = T\cos\varphi$, the expressions for N_A follows Eq. (5). As shown in Figure 3(c) and (d), the intersections of rods on slip plane are of elliptical shape, which is approximated by a circle [15] with the diameter

$$d_P = \frac{D}{\sqrt{\cos\varphi}}. \tag{49}$$

Assuming a triangular array distribution of precipitates on the slip plane, the expressions for l_P and λ are

$$l_P = \sqrt{\frac{\pi D^2}{2\sqrt{3}f\cos\varphi}} \text{ and} \tag{50}$$

$$\lambda = l_P - D_P = l_P - \frac{D}{\sqrt{\cos\varphi}}. \tag{51}$$

In the case of c-axis rods intersected by Py-2 plane, $\varphi = 45.6°$, we obtain

$$\lambda = 1.139\sqrt{\frac{D^2}{f}} - 1.196\,D \text{ and} \tag{52}$$

$$\Delta\tau = \frac{Gb}{2\pi\sqrt{1-\nu}} \frac{1}{1.139\sqrt{\frac{D^2}{f}} - 1.196\,D} \ln\frac{1.196\,D}{r_0}. \tag{53}$$

2.4.2 First-order pyramidal slip plane $\{10\bar{1}1\}$

When the c-axis rods are intersected by Py-1 slip plane, the same set of equations Eq. (49-51) applies, λ and $\Delta\tau$ are calculated by

$$\lambda = 1.202\sqrt{\frac{D^2}{f}} - 1.263\ D \text{ and} \tag{54}$$

$$\Delta\tau = \frac{Gb}{2\pi\sqrt{1-\nu}} \frac{1}{1.202\sqrt{\frac{D^2}{f}} - 1.263\ D} \ln\frac{1.263\ D}{r_0}. \tag{55}$$

2.4.3 Prismatic slip plane

The c-axis rods precipitate are parallel to the prismatic slip plane, the probability of intersection is given by $P = D$, and the projection of the intersected precipitates on slip plane has a rectangular shape with length $T_P = T$ and width $D_P = \pi/4\ D$. It has the similar planar geometry as the basal precipitate plates intersected by prismatic slip plane (Figure 3b). Using $\varphi = 90°$ in Eq. (38) gives

$$l_P = \sqrt{\frac{\pi DT}{2\sqrt{3}f}} = 0.952\sqrt{\frac{DT}{f}}\,. \tag{56}$$

Substituting $T_P = T/\sin\varphi$ in Eq. (39) by D_P, and D_P in Eq. (40) by $T_P = T$, we obtain

$$\lambda_1 = \sqrt{\left(l_p \sin 60° - D_P\right)^2 + \left(l_p \cos 60°\right)^2}, \tag{57}$$

$$\lambda_2 = l_P - T \text{ and} \tag{58}$$

$$\lambda_{eff} = \sqrt{0.403\frac{DT}{f} - 0.576\ D\sqrt{\frac{DT}{f}} + 0.274\ D^2}\ + 0.317\sqrt{\frac{DT}{f}} - 0.333\ T. \tag{59}$$

The increment of CRSS is

$$\Delta\tau = \frac{Gb}{2\pi\sqrt{1-\nu}} \frac{1}{\sqrt{0.403\frac{DT}{f} - 0.576\ D\sqrt{\frac{DT}{f}} + 0.274\ D^2\ + 0.317\sqrt{\frac{DT}{f}} - 0.333\ T}} \ln\frac{0.886\sqrt{DT}}{r_0} \tag{60}$$

3. Strengthening of slip systems by each type of precipitate

The formulae developed above show that the increment in the CRSS of a selected slip system by each type of precipitates has a distinct dependence upon the precipitate volume

fraction f, diameter D and thickness (or length) T. Figure 4 presents the strengthening effects of the four types of precipitates on all the slip systems in Mg alloys with respect to volume fraction f. At a given volume fraction, the CRSS increment of a slip system due to each type of precipitate is normalized by that due to a spherical precipitate of the same volume fraction. The calculations were performed for two aspect ratios $q = 10$ and 50 ($q = D/T$ for plate and $q = T/D$ for rod), and the volume of each individual precipitate at all values of f and q is kept at a constant value. For example, at $q = 10$, the dimensions of $D = 20$ nm, $T = 2$ nm for plate or $D = 4.3$ nm, $T = 43$ nm for rod as experimentally characterized in some Mg alloys [6, 17]. are employed. Precipitates may overlap on the slip plane with increasing volume fraction, especially at large aspect ratio. In that case, the data is truncated in the plot, e.g. in Figure 4(g). For the purpose of comparison, the strengthening effects of the precipitates on the basal slip system were included, following the formulae provided in [9].

The plots in Figure 4 show that, in general, non-spherical precipitates are stronger strengtheners than spherical ones, with the exceptions of basal plates against basal slip system, and c-axis rods against the prismatic slip system (Figure 4c, d at $q = 10$ and g, h at $q = 50$). The weaker strengthening effects in the latter two cases arise from the lower probability of the precipitates being intersected by slip plane, since their directions of larger dimension are parallel to the slip plane. For the same reason, larger aspect ratios of basal plates and c-axis rods result in weaker strengthening for basal and prismatic slip systems respectively, as in contrast to other combinations of precipitate and slip system, whose normalized CRSS increments are larger at $q = 50$.

Among the four precipitate morphologies, the prismatic plates generally produce higher normalized CRSS increment. The geometric models in the previous section suggest that because of the multiplicity of prismatic planes, the projection of the intersected precipitates are rectangles at different angles, they can potentially form closed zones on slip plane, therefore lead to rapidly increasing value of $\Delta\tau$ with increasing f and q of precipitates. It was envisioned by Nie that a continuous network of prismatic and basal precipitate plates can divide a grain into blocks and therefore contribute to achieving high strength [1]. In the case of basal plates and c-axis rods, the projections on slip plane are parallel rectangles or ellipses, there is always a relatively open area between rows of parallel rectangles for easier dislocation glide even at large f or q values when precipitates may overlap at the tip of rectangles (Figure 1b compared to Figure 3b). The CRSS

increments due to basal plates and c-axis rods increase slowly with volume fraction, at a similar rate as spherical precipitates, therefore the normalized $\Delta\tau$ changes only slightly in the plots (e.g. Figure 4c and d).

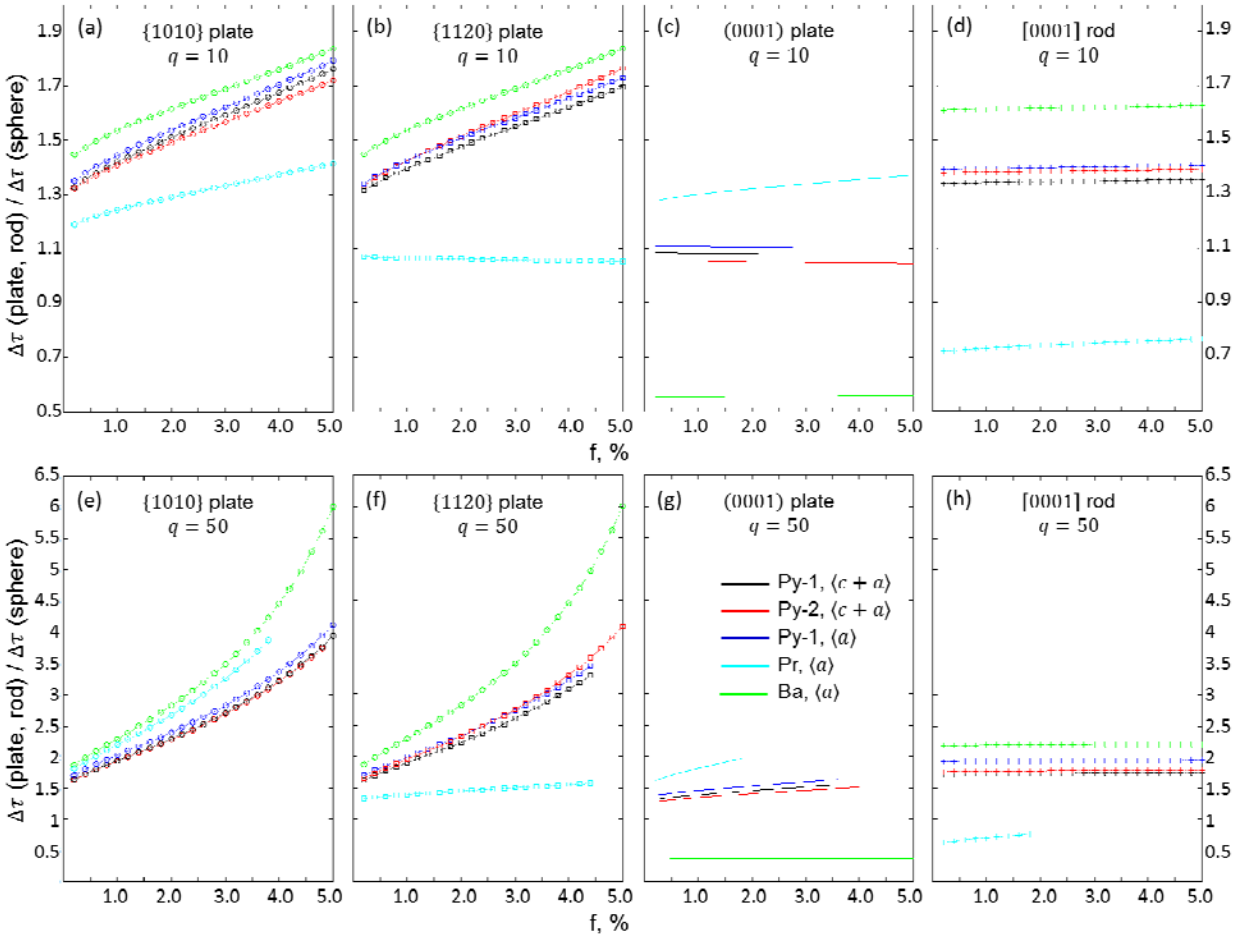

Figure 4. Variation of the normalized $\Delta\tau$ with volume fraction for five slip systems strengthened by (a) and (e) $\{10\bar{1}0\}$ plate, (b) and (f) $\{11\bar{2}0\}$ plate, (c) and (g) (0001) plate, (d) and (h) $[0001]$ rod. The slip systems are represented by curves in different colors as indicated in (g). Two aspect ratios of precipitates are used $q = 10$ (a-d) and $q = 50$ (e-h).

The Orowan strengthening effects of precipitates on prismatic slip system have been investigated by Robson [10, 18]. The modifications in the current model for prismatic slip system as compared to that of Robson include the adoptions of (1) a triangular array distribution of precipitate on slip plane and (2) the averaged λ of the nearest neighbors of precipitates. The results show that the prismatic $\langle a \rangle$ slip system is strengthened the most effectively by $\{10\bar{1}0\}$

plates in comparison to spherical particles. Between the two types of prismatic plates, $\{10\bar{1}0\}$ plates produce invariantly larger CRSS increment for prismatic slip as compared to $\{11\bar{2}0\}$ plates, for all the volume fraction and aspect ratios used. This is similar to the comparison between the effects of $\{111\}$ and $\{100\}$ plates on impeding the $\{111\}$ slip system in fcc structured metals (e.g. Al alloys [16]). In both crystal structures, the plates lying on the slip plane are the more effective strengthener. The c-axis rods result in the lowest normalized CRSS increments. It is partly due to the small particle size used in the current calculation: $D = 4.3$ nm and $T = 43$ nm at $q = 10$. Robson [18] showed that with a larger effective particle size, the c-axis rods are the least effective among the four types of precipitates at low volume fraction and become the strongest at high volume fraction. On the other hand, the average λ is used in this work rather than the smallest one. It can be expected that at large aspect ratio or volume fraction, the rods have very small end to end spacing which leads to rapid increase in $\Delta\tau$ if considering only this distance.

The pyramidal $\langle c + a \rangle$ and $\langle a \rangle$ slip systems are strengthened more effectively by prismatic plate precipitates, and the least by (0001) basal plates. The $\langle c + a \rangle$ dislocations on two pyramidal planes experience similar CRSS increments by each type of precipitate at a given volume fraction. The difference arises from the slightly different geometric factors in the expression of $\Delta\tau$ (e.g. Eq. (14) and (18)). When the volume fraction is very small, the c-axis rods have a larger probability of being intersected by the slip plane, they introduce larger CRSS increment than prismatic plates.

Figure 4 suggests that prismatic plates generally produce higher normalized CRSS increments. The following is an example of how to employ the relationships contained within this paper. In Mg alloy, WE43-T5 plate (hot rolled and artificially aged), precipitate plates on both prismatic planes as well as globular precipitates are present [19]. In what follows, the resultant absolute CRSS increment of all slip systems are evaluated with a fixed precipitate volume, as a function of volume fraction. As shown in Figure 5, the pyramidal $\langle c + a \rangle$ slip systems obtain the largest CRSS increment, followed by basal, pyramidal and prismatic $\langle a \rangle$ slip systems in sequence. It should be noted that the larger increment in $\langle c + a \rangle$ slip systems is simply due to the larger magnitude of the Burgers vector, as compared to those involving dislocations with $\langle a \rangle$ Burgers vector. In fact, with the same Burgers vector, Py-1 $\langle a \rangle$ slip system gains a slightly lower CRSS increment than the basal $\langle a \rangle$ slip system (compare the blue curves

and green curve in Figure 5). At large volume fractions, e.g. $f = 3\%$, the CRSS increments for $\langle c + a \rangle$ slip systems are larger than 200 MPa, and those for basal and prismatic slip systems are 144 MPa and 114 MPa respectively. Whereas these values indicate a high strength improvement solely due to Orowan hardening, a caveat is put forward that the effective volume fraction of the strengthening precipitates may be much lower than the global volume fraction measured experimentally [19]. On the other hand, the size limit of shear resistant precipitates is unclear for certain phases, so the values may exceed the strengthening capability of precipitate.

4. The $\langle c + a \rangle$ dislocation slip in the $\{10\bar{1}2\}$ twin in Mg alloys

It has been shown in the Mg alloy AZ31 compressed along the rolling direction, that the activated $\{10\bar{1}2\}$ twins contain abundant $\langle c + a \rangle$ dislocations resulting from the dislocation transmutation mechanism [13]. Whereas the slip activity of these dislocations affects significantly the hardening behavior of the material [12], the strengthening of the $\langle c + a \rangle$ slip systems inside twin due to the aforementioned precipitates is discussed subsequently. Following the notations in [13], the $(10\bar{1}2)$ twin contains only $\langle c \pm a_2 \rangle$ dislocations due to the transmutation mechanism. Taking the $[c + a_2]$ dislocation as an example, by using the lattice correspondence matrix developed by Niewczas [20] and neglecting the small rotation (~4°) that the precipitates undergo during twinning [3, 10], the following conclusions can be drawn.

Figure 6 presents the strengthening effects of the four types of precipitates on the first order and second order pyramidal $\langle c \pm a_2 \rangle$ slip systems inside twin. The Py-1, $\langle c \pm a_2 \rangle$ slip systems are strengthened the most effectively by $\{10\bar{1}0\}$ plates, the least by basal plates. It experiences larger CRSS increments than the Py-2, $\langle c \pm a_2 \rangle$ slip systems by a given type of precipitates, except for basal plates. For Py-2, $\langle c \pm a_2 \rangle$ slip systems, $\{10\bar{1}0\}$ plate and basal plates are the most effective strengtheners. And there is a transition volume fraction above which the $\{10\bar{1}0\}$ plates become better strengthener. Taking into account the strengthening effect of precipitates in matrix, it suggests that the $\{10\bar{1}0\}$ plates overall lead to the largest CRSS increments for dislocation slip in both matrix and twin. Note that Robson et al. [18] performed a similar analysis for basal slip within twins already and they found that it is the most effectively strengthened by basal plates, followed by prismatic plates, and the least by c-axis rods.

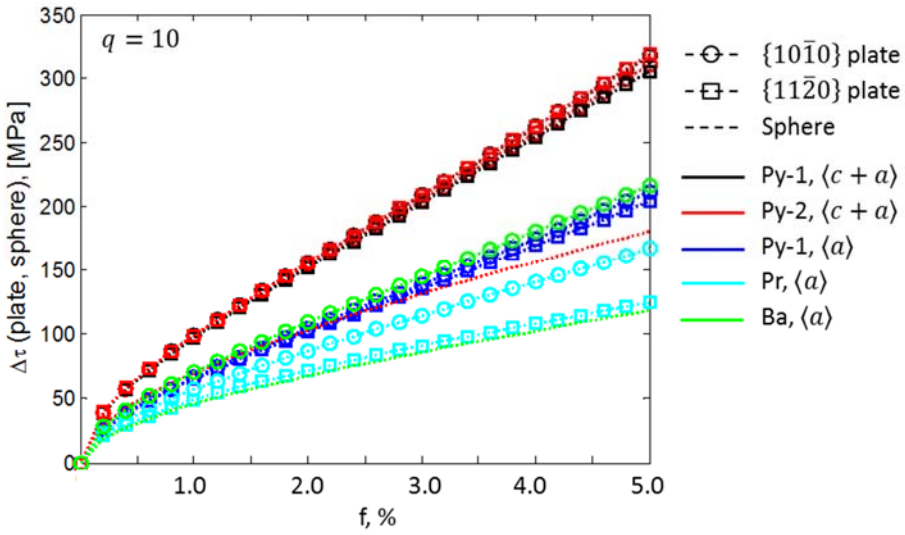

Figure 5. CRSS increment of slip systems due to Orowan strengthening by $\{10\bar{1}0\}$ and $\{11\bar{2}0\}$ plate and spherical precipitates, as observed in Mg alloy, WE43-T5 [19]. The three precipitate morphologies are represented by marker shapes circle, square and no marker respectively. The five slip systems are represented by different colors of markers and dashed lines. Plate size is $D = 20$ nm and $T = 2$ nm, spheres have the same volume as plate precipitates.

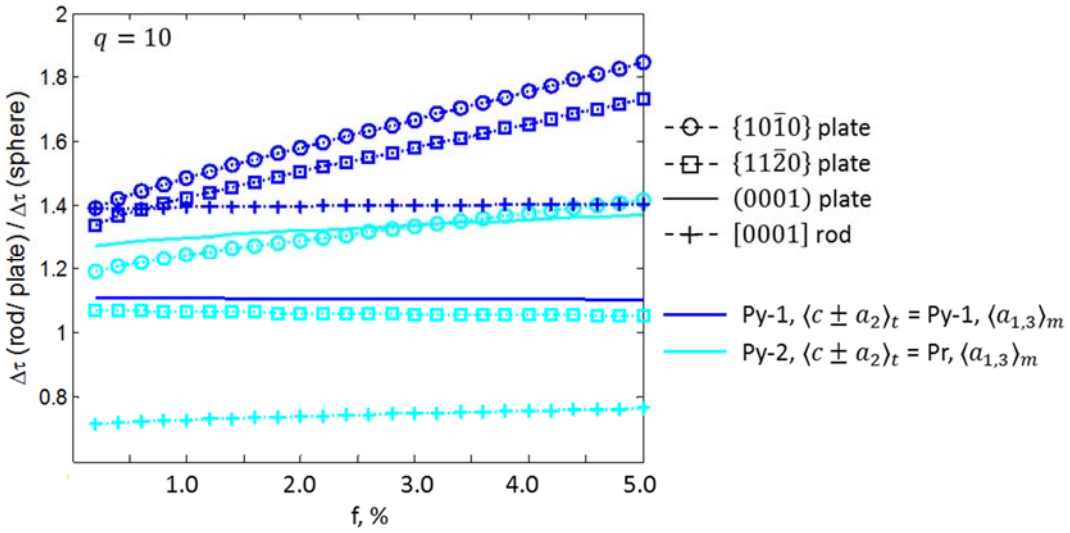

Figure 6. Variation of the normalized CRSS increment with the volume fraction of four precipitates, whose aspect ratio q is 10. The slip systems considered inside twin comprise the transmuted $\langle c \pm a_2 \rangle$ dislocations on first order (Py-1) and second order (Py-2) pyramidal planes.

5. Conclusions

In the current work, the Orowan equations for non-basal slip system were developed, based on the assumption of a triangular array distribution of precipitates on slip plane and the adoption of the average inter-particle spacing λ. On one hand, this scheme takes into account the probability of a dislocation experiencing different obstacle variants and spacings. On the other hand, it may deviate from the real case where the effective inter-particle spacing may be much more variable and there are other values which are important [3], e.g., an edge $\langle a \rangle$ dislocation on prismatic plane will likely bow out at the smallest end-to-end spacing of c-rods (λ_2 in Figure 3b), and a screw $\langle a \rangle$ dislocation will be obstructed by the larger spacing λ_1. In this case, one should select the appropriate inter-particle spacing rather than the weighted average. The relationships in this paper provide researchers with the necessary starting point for these more detailed considerations. In a recent crystal plasticity modeling work on Mg alloy WE43 [19], the equations were incorporated to quantitatively evaluate the strengthening effects of different precipitate geometry on various slip modes, and achieved good agreement with the macroscopic hardening.

Calculations using the provided formulae suggest that the $\langle c + a \rangle$ slip systems are generally strengthened the most effectively by $\{10\bar{1}0\}$ and $\{11\bar{2}0\}$ prismatic precipitate plates. Only at very low volume fraction (< 0.4 Vol.%), c-axis precipitate rods become the more effective strengthener. For example, if the prismatic precipitate plates have the size of $D = 20$ nm and $T = 2$ nm at volume fractions below 5%, they introduce the largest CRSS increment to $\langle c + a \rangle$ slip system, followed by basal and prismatic slip systems in sequence. This large effect on $\langle c + a \rangle$ slip owes largely to the large Burgers vector of the dislocations.

Assuming the effect of twinning shear is negligible since it only rotates the precipitates by about 4°, the effects of differently shaped precipitates on the $\langle c + a \rangle$ slip inside the $\{10\bar{1}2\}$ twins were evaluated by transforming the slip systems inside twin to those in the matrix. This analysis suggests that overall the $\{10\bar{1}0\}$ precipitate plates introduce the largest CRSS increment to $\langle c + a \rangle$ dislocation slip on first and second order pyramidal planes inside twin.

Finally, although the precipitates discussed in the current work stem from Mg alloys, the equations are applicable for other hcp metals (e.g. Ti and Zr), if the precipitates with the same morphologies are present.

Acknowledgements

The authors would like to acknowledge J.D. Robson at Manchester Materials Science Centre for discussions on developing the geometric models of prismatic plate shaped precipitates. The present work was sponsored by the National Science Foundation, grant number CMMI 1235259 (Mary Toney), as well as the U.S. Army Research Office under contract number W911NF-12-1-0455 (Suveen Mathaudhu and David Stepp). The views and conclusions contained in this document are those of the authors and should not be interpreted as representing the official policies, either expressed or implied, of the Army Research Laboratory or the U.S. Government.

Appendix

The angle φ between two planes $(h_1\ k_1\ i_1\ l_1)$ and $(h_2\ k_2\ i_2\ l_2)$ are calculated by equations in [21].

$$\cos\varphi = 4\,n_1 n_2\,a^{-2}\left[h_1h_2 + k_1k_2 + i_1i_2 + \frac{1}{2}(h_1k_2 + h_1i_2 + k_1i_2 + k_1h_2 + i_1h_2 + i_1k_2) + \gamma^{-2}l_1l_2\right]/3$$

where a is the lattice constant, $\gamma = c/a$, and n is the interplanar spacing of planes calculated from $n = a\left[\frac{4}{3}(h^2 + k^2 + i^2 + hk + ki + ih) + \gamma^{-2}l^2\right]^{1/2}$.

Table 1. The angles between the precipitate plane and slip plane in Mg ($c/a = 1.624$). The inter-planar angles are calculated by using the equations above.

Precipitate – slip plane	Angle between planes		Base angle of the isosceles triangle formed by the intersected precipitates
$\{10\bar{1}0\}_P$ - $\{11\bar{2}2\}_{slip}$	$\varphi_1 = 90°$ $(1\bar{1}00)$ to $(11\bar{2}2)$	$\varphi_2 = 42.5°$ $(10\bar{1}0)$ and $(01\bar{1}0)$ to $(11\bar{2}2)$	$\theta = 42.2°$ $\theta = \text{acos}\dfrac{\sqrt{\gamma^2+1}/2}{\sqrt{\left(\frac{\gamma}{2}\right)^2+1}}$
$\{10\bar{1}0\}_P$ - $\{10\bar{1}1\}_{slip}$	$\varphi_1 = 28.1°$ $(01\bar{1}0)$ to $(01\bar{1}1)$	$\varphi_2 = 63.8°$ $(10\bar{1}0)$ and $(1\bar{1}00)$ to $(01\bar{1}1)$	$\theta = 74.8°$ $\theta = \text{acos}\left(\dfrac{1/2}{\sqrt{\gamma^2+1}}\right)$

$\{10\bar{1}0\}_P$ - $\{10\bar{1}0\}_{slip}$	$\varphi_1 = 0°$ * $(10\bar{1}0)$ to $(10\bar{1}0)$	$\varphi_2 = 60°$ * $(01\bar{1}0)$ and $(1\bar{1}00)$ to $(10\bar{1}0)$	$\theta = 60°$ *
$\{11\bar{2}0\}_P$ - $\{11\bar{2}2\}_{slip}$	$\varphi_1 = 31.6°$ $(11\bar{2}0)$ to $(11\bar{2}2)$	$\varphi_2 = 64.8°$ $(1\bar{2}10)$ and $(\bar{2}110)$ to $(11\bar{2}2)$	$\theta = 73.2°$ $\theta = \text{acos}\left(\frac{\frac{\sqrt{3}}{2}}{\sqrt{\frac{9}{4}\gamma^2 + 3}}\right)$
$\{11\bar{2}0\}_P$ - $\{10\bar{1}1\}_{slip}$	$\varphi_1 = 90°$ $(\bar{2}110)$ to $(01\bar{1}1)$	$\varphi_2 = 40.2°$ $(11\bar{2}0)$ and $(1\bar{2}10)$ to $(01\bar{1}1)$	$\theta = 39.2°$ $\theta = \text{acos}\left(\frac{\sqrt{3+4\gamma^2}/2}{\sqrt{3+\gamma^2}}\right)$
$\{11\bar{2}0\}_P$ - $\{10\bar{1}0\}_{slip}$	$\varphi_1 = 90°$ * $(1\bar{2}10)$ to $(10\bar{1}0)$	$\varphi_2 = 30°$ * $(11\bar{2}0)$ and $(\bar{2}110)$ to $(10\bar{1}0)$	$\theta = 60°$ *
$\{0001\}_P$ - $\{11\bar{2}2\}_{slip}$	$\varphi = 45.6°$		$\theta = 60°$ *
$\{0001\}_P$ - $\{10\bar{1}1\}_{slip}$	$\varphi = 51.1°$		$\theta = 60°$ *
$\{0001\}_P$ - $\{10\bar{1}0\}_{slip}$	$\varphi = 90°$		$\theta = 60°$ *

*: the angle is independent of c/a ratio.

References

[1] J. Nie, "Precipitation and hardening in magnesium alloys," *Metallurgical and materials transactions A,* vol. 43A, pp. 3891-3939, 2012.

[2] S. Celotto, "TEM study of continuous precipitation in Mg-9 wt% Al-1 wt% Zn alloy," *Acta Materialia,* vol. 48, pp. 1775-1787, 2000.

[3] N. Stanford and M. Barnett, "Effect of particles on the formation of deformation twins in a magnesium-based alloy," *Materials Science and Engineering A,* vol. 516, pp. 226-234, 2009.

[4] J. Jain, P. Cizek, W. Poole and M. Barnett, "Precipitate characteristics and their effect on the

prismatic-slip-dominated deformation behaviour of an Mg-6Zn alloy," *Acta Materialia,* vol. 61, pp. 4091-4102, 2013.

[5] C. Mendis, C. Bettles, M. Gibson, S. Gorsse and C. Hutchinson, "Refinement of precipitate distributions in an age-hardenable Mg-Sn alloy through microalloying," *Philosophical Magazine Letters,* vol. 86, pp. 443-456, 2006.

[6] C. Mendis, K. Oh-ishi, Y. Kawamura, T. Honma, S. Kamado and K. Hono, "Precipitation-hardenable Mg-2.4Zn-0.1Ag-0.1Ca-0.16Zr (at.%) wrought magnesium alloy," *Acta Materialia,* vol. 57, pp. 749-760, 2009.

[7] J. Wang and N. Stanford, "Investigation of precipitate hardening of slip and twinning in Mg5%Zn by micropillar compression," *Acta Materialia,* vol. 100, pp. 53-63, 2015.

[8] C. Antion, P. Donnadieu, F. Perrard, A. Deschamps, C. Tassin and A. Pisch, "Hardening precipitation in a Mg-4Y-3RE alloy," *Acta Materialia,* vol. 51, pp. 5335-5348, 2003.

[9] J. Nie, "Effects of precipitate shape and orientation on dispersion strengthening in magnesium alloys," *Scripta Materialia,* vol. 48, pp. 1009-1015, 2003.

[10] J. Robson, N. Stanford and M. Barnett, "Effect of precipitate shape on slip and twinning in magnesium alloys," *Acta Materialia,* vol. 59, pp. 1945-1956, 2011.

[11] S. Agnew, R. Mulay, F. Polesak III, C. Calhoun, J. Bhattacharyya and B. Clausen, "In situ neutron diffraction and polycrystal plasticity modeling of a Mg–Y–Nd–Zr alloy: Effects of precipitation on individual deformation mechanisms," *Acta Materialia,* vol. 61, pp. 3769-3780, 2013.

[12] H. El Kadiri and A. Oppedal, "A crystal plasticity theory for latent hardening by glide twinning through dislocation transmutation and twin accommodation effects," *Journal of the Mechanics and Physics of Solids,* vol. 58, pp. 613-624, 2010.

[13] F. Wang and S. Agnew, "Dislocation transmutation by tension twinning in magnesium alloy AZ31," *International Journal of Plasticity*, vol. 81, pp. 63-86, 2016.

[14] A.J. Ardell, "Precipitation hardening," *Metallurgical Transactions A*, vol. 16A, pp. 2131-2165, 1985.

[15] R. Fullman, Trans AIME, vol. 197, pp. 447-452, 1953.

[16] J. Nie, B. Muddle and I. Polmear, "The effect of precipitate shape and orientation on

dispersion strengthening in high strength aluminium alloys," *Materials Science Forum,* Vols. 217-222, pp. 1257-1262, 1996.

[17] R. Wilson, C. Cettles, B. Muddle and J. Nie, "Precipitation hardening in Mg-3 wt% Nd (-Zn) casting alloys," *Materials Science Forum,* Vols. 419-422, pp. 267-272, 2003.

[18] J. Robson, "The effect of precipitate morphology and habit on strengthening in magnesium alloys," in Mg2012: 9th international conference on magnesium alloys and their applications. W.J. Poole and K.U. Kainer, 2012.

[19] J. Bhattacharyya, et al., "Demonstration of alloying, thermal activation, and latent hardening effects on quasi-static and dynamic polycrystal plasticity of Mg alloy, WE43-T5, plate," *International Journal of Plasticity,* vol. 81, pp. 123-151, 2016.

[20] M. Niewczas, "Lattice correspondence during twinning in hexagonal close-packed crystals," Acta Materialia, vol. 58, pp. 5848-5857, 2010.

[21] H. Otte and A. Crocker, "Crystallographic formulae for hexagonal lattices," *Phys. Stat. Sol.,* vol. 9, pp. 441-450, 1965.